



Cite this: DOI: 10.1039/d0en00801j

Few-layered tungsten selenide as a co-catalyst for visible-light-driven photocatalytic production of hydrogen peroxide for bacterial inactivation†

Wanjun Wang, Wenquan Gu, Guiying Li,  Haojing Xie,
Po Keung Wong  and Taicheng An *

Sustainable and “green” technologies for hydrogen peroxide (H_2O_2) production have aroused increasing interest, yet challenges prevail in production of H_2O_2 for environmental applications. In this study, tungsten selenide (WSe_2) with a few-layered microstructure was used as a new co-catalyst to synthesize H_2O_2 under visible light irradiation. The ultrathin WSe_2 nanosheets were anchored onto a $\text{g-C}_3\text{N}_4$ surface by *in situ* growth solvothermal methods. The as-prepared $\text{WSe}_2/\text{g-C}_3\text{N}_4$ showed remarkably enhanced H_2O_2 production efficiency without organic electron donors, which was 11.8 times higher than that of pristine $\text{g-C}_3\text{N}_4$. H_2O_2 was generated *via* O_2 reduction mediated by photogenerated e^- , and dissolved O_2 could be generated by water oxidation and *in situ* used to produce H_2O_2 under anaerobic conditions. The introduction of WSe_2 not only promoted visible light absorption, but also facilitated the charge transfer efficiency by forming a Z-scheme rather than a type II heterojunction. The photogenerated e^- was enriched onto WSe_2 , leading to the high H_2O_2 production activity. Moreover, the *in situ* generated H_2O_2 could be directly used for pathogenic bacteria inactivation through Fenton reactions without external H_2O_2 addition. This work is expected to open an avenue for developing novel photocatalysts towards sustainable H_2O_2 production for water disinfection and related environmental applications.

Received 1st August 2020,
Accepted 9th October 2020

DOI: 10.1039/d0en00801j

rsc.li/es-nano

Environmental significance

H_2O_2 as a “green” oxidant is of vital importance to advanced oxidation processes (AOPs) in the environmental field. However, large-scale application of H_2O_2 -based Fenton processes is restrained by the high-cost production of H_2O_2 and the difficulties in the transfer and storage of liquid H_2O_2 . This study presented the utilization of solar energy for direct production of H_2O_2 through the introduction of photocatalysts by applying few-layered WSe_2 as co-catalysts. The generated H_2O_2 can also be combined with iron catalysts to construct *in situ* Fenton systems without addition of external H_2O_2 , thus solving the problem of H_2O_2 production and storage. The newly constructed *in situ* Fenton systems are expected to be used for various environmental applications including pollutant degradation and inactivation of pathogenic microorganisms, such as bacteria and viruses.

1. Introduction

Hydrogen peroxide (H_2O_2) as an environmentally benign oxidant has been widely used in organic pollutant degradation and pathogenic bacteria inactivation.^{1–3}

Guangdong Key Laboratory of Environmental Catalysis and Health Risk Control, Guangzhou Key Laboratory Environmental Catalysis and Pollution Control, School of Environmental Science and Engineering, Institute of Environmental Health and Pollution Control, Guangdong University of Technology, Guangzhou 510006, China. E-mail: antc99@gdut.edu.cn; Tel: +86 20 3932 2298

† Electronic supplementary information (ESI) available: Experimental details (fabrication of WSe_2 nanosheets, characterization of materials, photoelectrochemical measurements, H_2O_2 measurements); wavelength dependent photocatalytic H_2O_2 evolution; evolution of dissolved O_2 ; nitrogen adsorption-desorption isotherms and pore size distribution; RDE measurements; Mott-Schottky plots; and fluorescence spectra of coumarin with and without $\text{Fe}(\text{II})$ addition to the CNW/VL system. See DOI: 10.1039/d0en00801j

However, H_2O_2 is traditionally produced using the anthraquinone process, which suffers from high energy consumption.⁴ In addition, the direct synthetic routes using H_2 and O_2 in the presence of noble metal catalysts involve high risk, due to the explosive nature of the H_2/O_2 mixture.⁵ Therefore, safer and “green” methods for the production of H_2O_2 are highly desired and have recently attracted increasing attention worldwide.⁶

The semiconductor photocatalytic reaction has been regarded as one of the most promising technologies for H_2O_2 synthesis due to the utilization of sustainable sunlight as the energy source.⁷ In a photocatalytic process, O_2 is captured by photogenerated electrons from an excited semiconductor, and undergoes a two-electron reduction process to produce H_2O_2 ,⁸ avoiding the use of conventional methods of the explosive H_2/O_2 mixture. However, the most widely used

photocatalyst for H₂O₂ production is TiO₂, which is only active under UV irradiation. In addition, noble metals are often used as co-catalysts.⁹ For example, Tsukamoto *et al.* have reported that the H₂O₂ production rate by pure TiO₂ is low, and can be significantly enhanced by loading with Au–Ag alloys.¹⁰ Moreover, H₂O₂ also suffers from decomposition under UV irradiation.¹¹ In this regard, visible-light driven (VLD) photocatalysts for H₂O₂ production have been an intensively pursued topic in recent years. Among these identified VLD photocatalysts, graphitic carbon nitride (g-C₃N₄), being widely used as a prospective photocatalyst for pollutant degradation,¹² water disinfection,^{13–15} H₂ production¹⁶ and CO₂ reduction,¹⁷ has also been found to possess high activity towards H₂O₂ production.^{18,19} For example, Shiraishi *et al.* have found a superior efficiency of H₂O₂ production over g-C₃N₄ to TiO₂, due to the formation of 1,4-endoperoxide species on g-C₃N₄, which facilitates the subsequent H₂O₂ production.²⁰ However, in most of the photocatalytic H₂O₂ production systems including g-C₃N₄, sacrificial agents are always needed and H₂O₂ is often produced with electron donors (*i.e.* ethanol, isopropanol, *etc.*).^{20–26} The use of earth-abundant water replacing alcohols for photocatalytic H₂O₂ synthesis will fulfill the concept of clean and sustainable production. However, developing highly efficient photocatalytic systems which can produce H₂O₂ in pure water is still a challenge.²⁷ To this end, it is very attractive to develop alternative noble-metal-free co-catalysts to promote the H₂O₂ production in pure water systems.

Recently, transition metal dichalcogenides (TMDs) have attracted boosting interest worldwide due to their layered crystal structure, high chemical stability and excellent electrochemical properties.²⁸ Tungsten selenide (WSe₂), as a typical TMD widely used in solar cells²⁹ and gas sensors,³⁰ has also found great applications in photocatalytic water splitting³¹ and CO₂ reduction.³² Lin *et al.* reported that WSe₂ as a co-catalyst could improve the photocatalytic performance for photocatalytic water splitting by promoting electron–hole separation.³³ Duan *et al.* further found that WSe₂ exhibits tunable band gaps when the thickness is varied from bulk to a single layer.³⁴ The unique properties of small band gaps and layered crystal structures facilitate the high VL absorption and substance adsorption.^{35,36} Unfortunately, it is still unknown whether WSe₂ nanostructures could be used as co-catalysts for photocatalytic H₂O₂ production.

Meanwhile, pathogenic bacterial inactivation has been taken as a priority to improve water quality, as huge mortality occurred as a result of microbial contaminated water especially in developing countries. Bacterial inactivation using advanced oxidation processes (AOPs) as alternative disinfection methods has attracted increasing attention. In particular, the Fenton process is one of the most widely studied AOPs.³⁷ However, the traditional Fenton technology requires external oxidant (*i.e.* H₂O₂) addition, which inevitably increases the operation costs. Therefore, it would be interesting to utilize H₂O₂ generated by photocatalytic processes to continuously supply the oxidant needed in the

Fenton process. This synergistic effect for bacterial inactivation has not been investigated in previous studies.

Herein, WSe₂ with different layers was used as a co-catalyst for H₂O₂ production in a g-C₃N₄ photocatalytic system. In order to achieve efficient photocatalytic H₂O₂ production in pure water under VL irradiation, few layered WSe₂ was loaded onto g-C₃N₄ by a facile solvothermal method. The photocatalytic H₂O₂ generation efficiencies in pure water and alcohols were also compared, and the role of WSe₂ in the photocatalytic process was studied in detail. Moreover, a photo-Fenton system was constructed by using the *in situ* generated H₂O₂ combined with Fe(II) for bacterial inactivation without external addition of H₂O₂. To the best of our knowledge, there is no report about VLD photocatalytic H₂O₂ production using WSe₂ as a co-catalyst for bacterial inactivation. This work is expected to shed light on the design and fabrication of WSe₂-based photocatalysts for H₂O₂ production, thus advancing the areas of cleaner production *via* green and sustainable routes for environmental applications.

2. Experimental

2.1 Chemicals

Melamine (99%, Aladdin), sodium tungstate dihydrate (Na₂WO₆·2H₂O, 99.5%, Aladdin), *N,N*-dimethylformamide (DMF, 99.5%, Aladdin), selenium (99.9%, Aladdin), *N,N*-diethyl-*p*-phenylenediamine sulfate salt (DPD, C₁₀H₁₆N₂·H₂SO₄, 98%, Aladdin), sodium borohydride (NaBH₄, 98%, Aladdin), peroxidase from horseradish (POD, >200 units per mg, Aladdin) and ethanol (99.7%) were used as received without further purification.

2.2 Materials synthesis and characterization

Pristine g-C₃N₄ was prepared by thermal polymerization of melamine. 10 g melamine was placed in a crucible with a lid in a muffle furnace under a static air atmosphere and heated at 520 °C for 2 h with a heating rate of 2 °C min⁻¹. Then, the crucible was cooled to room temperature naturally. The resulting yellow product was collected and ground into fine powder for further use.

WSe₂/g-C₃N₄ hybrids with different WSe₂ loading amounts were synthesized by a modified solvothermal method.³⁸ Typically, to synthesize 10.4 wt% WSe₂/g-C₃N₄ (CNW-4), a stoichiometric ratio of elemental Se powder (1.54 mmol, 121.6 mg) and Na₂WO₆·2H₂O (0.772 mmol, 254 mg) was dissolved in 60 mL *N,N*-dimethylformamide (DMF) solution, followed by adding 100 mg NaBH₄ under vigorous stirring for 2 h. Subsequently, 2.5 g of pristine g-C₃N₄ was added to the above solution. The mixtures were vigorously stirred for 1 h, and then transferred into a 100 mL Teflon-lined autoclave and heated at 240 °C for 24 h. After cooling down to room temperature, the product was collected, washed with ethanol and distilled water several times, and dried in a vacuum at 60 °C for 24 h. Then the product was annealed at 300 °C for 5 h under an Ar atmosphere, and the final WSe₂/g-C₃N₄ product was obtained and denoted as CNW-4. To optimize

the efficiency, WSe₂/g-C₃N₄ samples with different weight ratios of WSe₂ (5.5%, 7.1%, 8.7%, 12% and 13.7%) were also synthesized by the same process, and denoted as CNW-1, CNW-2, CNW-3, CNW-5 and CNW-6, respectively.

To test whether the treatment with NaBH₄ in the preparation procedure would affect the photocatalytic properties of pristine g-C₃N₄, control experiments were added to synthesize bare g-C₃N₄ by the similar method in which only NaBH₄ was added (without Se powder and Na₂WO₆·2H₂O), and the obtained bare g-C₃N₄ product was denoted as BCN. In addition, pure WSe₂ was also synthesized by the similar method without the addition of pristine g-C₃N₄. The as-prepared samples were characterized by XRD, FTIR, SEM, TEM, BET, PL and electrochemical tests. Rotating disc electrode (RDE) tests were employed to investigate the number of electron transfer for O₂ reduction. The details of the synthetic procedure for WSe₂ and the characterization methods can be found in the ESI.†

2.3 Photocatalytic H₂O₂ production experiments

In a typical test, 50 mg of the as-prepared WSe₂/g-C₃N₄ was dispersed in 50 mL pure distilled water in a container with a cooling water jacket outside, followed by ultrasonic treatment for 1 min. The aqueous suspension was stirred in the dark for 20 min, and then irradiated by a 300 W Xe lamp with a UV cutoff filter ($\lambda > 420$ nm), while being continuously bubbled with an O₂ flow. The light intensity was fixed at 50 mW cm⁻² which was determined using a photometer (FZ-A, PerfectLight, China), and the reaction temperature was maintained at 25 °C during the experiments. At given time intervals, aliquots of the suspensions were taken from the reaction cell, and the produced concentrations of H₂O₂ were determined by the DPD/POD method according to the previous literature.³⁹ Briefly, 400 μ L of phosphate buffer, 1120 μ L of water, 1000 μ L of the filtered sample, 50 μ L of DPD solution and 50 μ L of POD solution were mixed and kept under vigorous stirring for 90 s. Then, the concentration of H₂O₂ was obtained by analyzing the absorbance at 551 nm using a microplate reader (Varioskan Lux, Thermo Scientific). The details for stock solution preparation (buffer solution, DPD, and POD) can be found in the ESI.† To calculate the apparent quantum yield (AQY), the incident light was obtained by using a band pass filter ($\lambda = 420$ nm), and the AQY was estimated by the following equation (eqn (1)):

$$\text{AQY(\%)} = \frac{(\text{number of H}_2\text{O}_2 \text{ molecules formed}) \times 2}{\text{number of incident photons}} \times 100 \quad (1)$$

2.4 Bacterial inactivation experiments

The bacterial inactivation was conducted using *Escherichia coli* (*E. coli*) as the model bacterium. In a typical experiment, *E. coli* cell suspension with a concentration of 1×10^7 cfu (colony forming unit) per mL and the as-prepared WSe₂/g-C₃N₄ (CNW-4) were mixed in a flask under stirring for 15

min. Then, an Fe(II) solution (FeSO₄, 2.7 mM) was added into the suspension with VL light irradiation to activate the *in situ* generated H₂O₂. At given time intervals, aliquots of the sample were collected and the viable cells were determined by the plate count method. The details of bacterial culture, harvesting, and determination procedures can be found in our previous studies.^{13–15} To study the *in situ* activation of H₂O₂, the \cdot OH generation was monitored using coumarin (1 mM) as the trapping agent, which was determined using a fluorescence spectrometer (Edinburgh FLS1000) at an emission wavelength of 460 nm with an excitation wavelength of 332 nm.⁴⁰

3. Results and discussion

3.1 Structure and morphology characterization

The XRD patterns in Fig. 1(A) show that the pristine g-C₃N₄ has two typical diffraction peaks centered at 13.1° and 27.6° respectively, which can be assigned to the (1 0 0) and (0 0 2) crystal facets of g-C₃N₄ respectively, in agreement with previous studies.^{41,42} In addition, the XRD peaks of the obtained WSe₂ can be well indexed to the typical hexagonal structure of WSe₂ (JCPDS No. 38-1388), suggesting that pure WSe₂ was successfully synthesized by the present solvothermal method without other impurities. For the as-prepared WSe₂/g-C₃N₄ composite samples, the positions of the diffraction peaks remained unchanged, indicating that the basic structure of g-C₃N₄ was not changed after loading with WSe₂. No characteristic diffraction peaks of WSe₂ can be observed, which is attributed to the weak crystallization and high dispersion of the anchored WSe₂ nanoparticles. In the FT-IR spectra (Fig. 1(B)), the pure WSe₂ shows almost no sharp peaks in the range of 650–3700 cm⁻¹, in agreement with a previous study.⁴³ For pristine g-C₃N₄, the sharp peak observed at 808 cm⁻¹ is attributed to typical vibration of triazine rings,⁴⁴ while the strong characteristic peaks in the range of 1100–1700 cm⁻¹ can be assigned to the stretching vibration of the C–N bond and C=N bond in heterocyclic g-C₃N₄ compounds.⁴⁵ In addition, the peaks located in the 3100–3400 cm⁻¹ region are attributed to the –NH₂ groups in the g-C₃N₄ structure.⁴⁶ It was noted that the peak positions of BCN (g-C₃N₄ treated with NaBH₄) were similar to those of pristine g-C₃N₄, suggesting that g-C₃N₄ treated with NaBH₄ alone would not change the molecular structure of g-C₃N₄. In addition, the as-prepared WSe₂/g-C₃N₄ composites also exhibited similar FT-IR spectral profiles with much lower peak intensity than those of pristine g-C₃N₄ and BCN, which could be obviously ascribed to the presence of black WSe₂ absorbing infrared light.⁴² The light harvesting properties were further studied by UV-vis absorption spectroscopy (Fig. 1(C)). Evidently, the pristine g-C₃N₄ and BCN exhibited typical absorption spectra with limited light absorption in the VL region ($\lambda < 450$ nm). Interestingly, the VL absorption wavelength was extended to 800 nm after loading with WSe₂ nanosheets on the surface of g-C₃N₄, due to the high VL absorption properties of WSe₂. With the increase of WSe₂

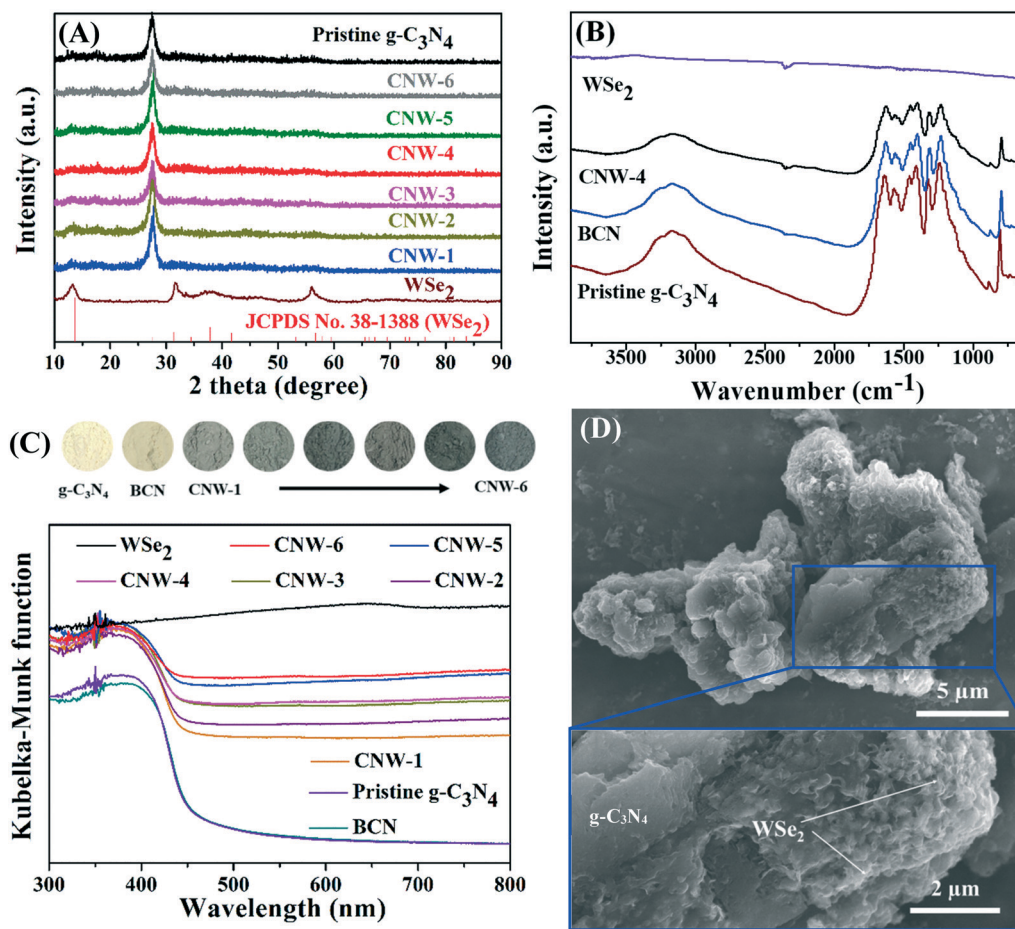


Fig. 1 (A) X-ray diffraction (XRD) patterns; (B) Fourier transform infrared (FT-IR) spectra; (C) UV-vis diffuse reflectance spectra (UV-vis DRS) of pristine $g\text{-C}_3\text{N}_4$, BCN, WSe_2 and $\text{WSe}_2/g\text{-C}_3\text{N}_4$ composites; (D) typical scanning electron microscopy (SEM) images of the CNW-4 composite.

loading amounts, the color of $g\text{-C}_3\text{N}_4$ was gradually changed from yellow to a dark color (Fig. 1(C) upper image), further confirming the existence of WSe_2 in the composites. The significantly enhanced light absorption would be beneficial to the photocatalytic H_2O_2 production efficiency.

The typical SEM image of the $\text{WSe}_2/g\text{-C}_3\text{N}_4$ composites shows that many ultra-thin WSe_2 nanosheets are grown on the surface of $g\text{-C}_3\text{N}_4$, indicating the successful fabrication of WSe_2 on $g\text{-C}_3\text{N}_4$ (Fig. 1(D)). The particle size of WSe_2 nanosheets attached onto the surface was much smaller than that of layered $g\text{-C}_3\text{N}_4$. In contrast, pure WSe_2 exhibits a hierarchical flower-like structure self-assembled from ultra-thin nanosheets, while pristine $g\text{-C}_3\text{N}_4$ and BCN exhibit a similar layered structure (Fig. S1†). To further confirm the existence of WSe_2 nanosheets on the surface of $g\text{-C}_3\text{N}_4$, TEM was conducted as shown in Fig. 2(A). Self-assembled nanosheets of WSe_2 were anchored onto the edge of $g\text{-C}_3\text{N}_4$ nanosheets, and the sizes of $g\text{-C}_3\text{N}_4$ nanosheets were observed to be much larger than that of WSe_2 nanosheets, in agreement with the above SEM image. The HR-TEM image in Fig. 2(B) further confirms 6 layers of nanosheets with an interlayer spacing of ~ 0.67 nm, which corresponds to the (002) planes of WSe_2 according to ref. 47. The HAADF image

and corresponding element mapping analysis demonstrate the presence of C, N, W and Se elements in the composites (Fig. 2(C)–(G)), and the amounts of W and Se were obtained to be 0.66 atom% and 1.34 atom%, respectively. The elemental ratio of W to Se was close to 1:2, confirming the successful synthesis of WSe_2 nanosheets onto $g\text{-C}_3\text{N}_4$ to form heterojunctions of binanosheets.

3.2 Photocatalytic H_2O_2 production

The photocatalytic H_2O_2 production experiments were conducted in pure water without any electron donors. As shown in Fig. 3(A), all the as-prepared samples exhibit different photocatalytic activities towards H_2O_2 production. In general, the H_2O_2 amounts increase with reaction time, and gradually slow down and tend to reach equilibrium, due to the simultaneous decomposition of H_2O_2 .⁵ The pristine $g\text{-C}_3\text{N}_4$ and pure WSe_2 show a rather limited activity, and only about $6.85 \mu\text{mol L}^{-1}$ and $10.71 \mu\text{mol L}^{-1}$ H_2O_2 were generated within 2 h. Interestingly, the CNW composites exhibit remarkably higher activity than pristine $g\text{-C}_3\text{N}_4$ and pure WSe_2 . Fig. 3(B) compares the H_2O_2 generation concentration within 2 h under VL irradiation. It was found that with

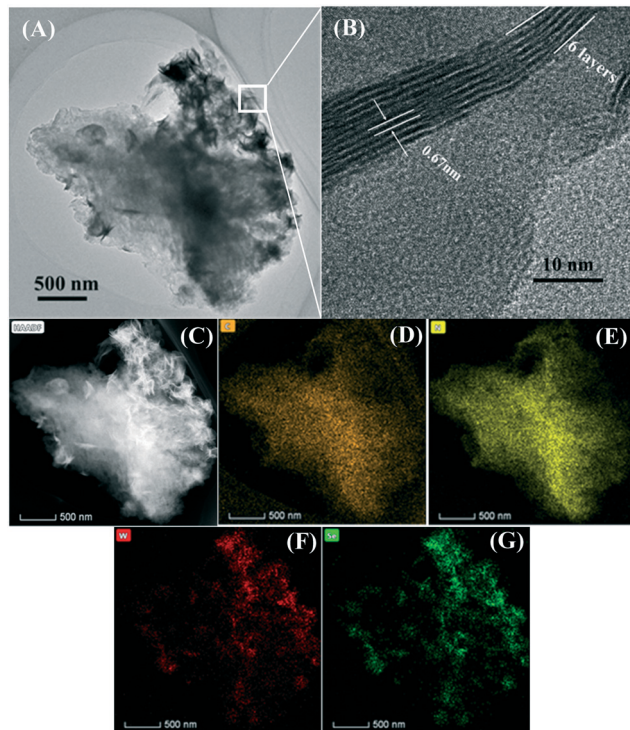


Fig. 2 (A) Transmission electron microscopy (TEM) image; (B) high resolution transmission electron microscopy (HR-TEM) image; (C) high-angle annular dark field (HAADF) image and (D)–(G) corresponding elemental mapping analysis.

increasing WSe₂ loading amount, the H₂O₂ generation efficiency was first increased and then decreased, probably because the excess WSe₂ would block light penetration to reach g-C₃N₄ and decrease the active sites of the catalyst. The highest activity was achieved for the CNW-4 sample, and the H₂O₂ generation could reach 81.24 μmol L⁻¹, which was 11.8 times higher than that of pristine g-C₃N₄.

A previous study has reported that the NaBH₄ treatment of g-C₃N₄ can lead to enhanced photocatalytic H₂O₂ production activity of g-C₃N₄ by creating N vacancies.⁴⁸ To verify whether the improvement of H₂O₂ production is caused by WSe₂ loading or by NaBH₄ treatment, control experiments were conducted using the bare g-C₃N₄ treated with NaBH₄ (BCN). Results show that BCN exhibits an enhanced H₂O₂ production concentration within the same 2 h (19.50 μmol L⁻¹) compared with pristine g-C₃N₄, but the efficiency is still much lower than CNW-4 (81.24 μmol L⁻¹). This result confirms that the *in situ* loading of WSe₂ as a co-catalyst is crucial to obtain the high H₂O₂ production efficiency. These results indicate that WSe₂ nanosheets could be new noble-metal-free co-catalysts for photocatalytic H₂O₂ production.

Table S1† compares the photocatalytic H₂O₂ production efficiency in different systems reported in this work as well as in early reported references. The CNW composites show superior H₂O₂ production efficiency to most of the reported photocatalytic systems, especially in pure water, suggesting their great potential for practical use. Moreover, the

wavelength-dependent photocatalytic H₂O₂ production was also studied using monochromatic light irradiation. Results showed that the VL responsive wavelength could be extended to 450 nm, which coincides with the VL absorption cutoff wavelength of WSe₂/g-C₃N₄ (Fig. S2†). The calculated apparent quantum yield (AQY) at 420 nm was 7.18% and 0.69% for WSe₂/g-C₃N₄ and pristine g-C₃N₄, respectively. Obviously, the AQY of photocatalytic H₂O₂ production over WSe₂/g-C₃N₄ is 10.4 times as high as that over pristine g-C₃N₄, which is also higher than the reported value (6.5%) obtained on polyoxometalate/g-C₃N₄.⁴⁹ It was also found that the H₂O₂ production efficiency could be further promoted by adding electron donors. As shown in Fig. 3(C), the H₂O₂ production is increased from 81.24 μmol L⁻¹ (pure water) to 151.77 μmol L⁻¹ within the same 2 h when adding 10% ethanol as the electron donor. This value was further increased to 240.08 μmol L⁻¹ when absolute ethanol (99.8%) was used, nearly 3.0 times higher than using pure water. This result also confirmed that H₂O₂ was produced *via* O₂ reduction by photogenerated e⁻ from the conduction band (CB) of the photocatalyst, which was different from some studies that H₂O₂ could be produced by photogenerated h⁺ from the valence band (VB).⁵⁰ Therefore, O₂ should be a crucial factor for the production activity of H₂O₂. However, it was interesting to find that the H₂O₂ generation was only slightly inhibited under simulated anaerobic conditions with N₂ aeration (Fig. 3(C)), suggesting that external O₂ is not so important in this photocatalytic system. This can be rationalized that the CNW composites can also serve as photocatalysts for O₂ evolution, since the VB potential of g-C₃N₄ is high enough to generate O₂.^{51,52} To support this assumption, dissolved O₂ in a sealed reactor was monitored during the reaction, and a steady increase in O₂ content was observed (Fig. S3†), suggesting that the CNW composites can really generate O₂ *in situ* which can be used for subsequent H₂O₂ production. These results suggest that the novel CNW system has potential to be used under anaerobic conditions to produce H₂O₂, thus further greatly expanding its application range in environmental remediation. To test the photostability, the used photocatalysts were recycled by centrifugation, washing and drying, and then three successive repeated experiments were examined. Fig. 3(D) shows that no obvious decline of H₂O₂ production efficiency over CNW-4 is observed within 50 min of VL irradiation during three cycles of H₂O₂ production. In addition, the crystal structure of CNW-4 remains unchanged before and after the reaction (Fig. S4†), indicating its good photostability and durability.

3.3 Enhanced mechanisms of H₂O₂ production

It is well known that the surface area plays a significant role in determining the photocatalytic activity. Therefore, the Brunauer–Emmett–Teller (BET) surface areas of the pristine g-C₃N₄, BCN and CNW-4 composite samples were evaluated. However, the BET surface areas of the three samples were less than 10 m² g⁻¹, which indicates that the excellent photocatalytic performance of CNW-4 did not originate from

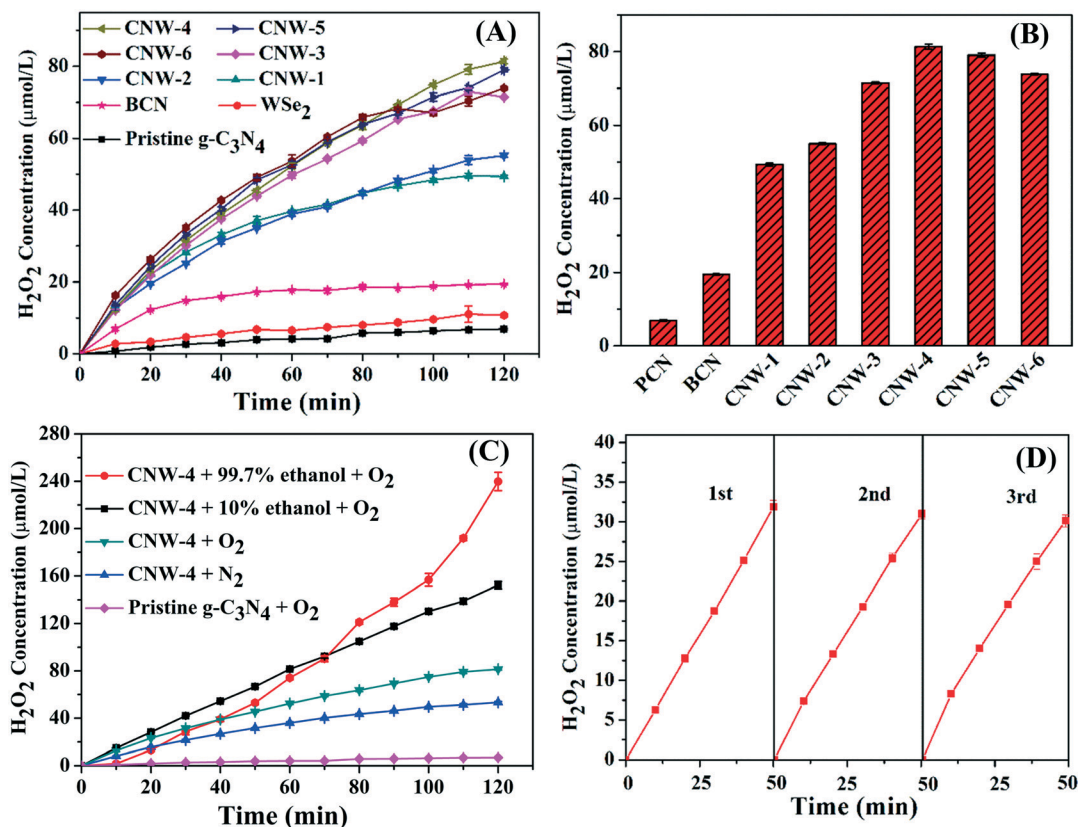


Fig. 3 (A) Photocatalytic H_2O_2 evolution over the as-prepared samples under VL irradiation; (B) comparison of H_2O_2 production over the different catalysts in 120 min; (C) photocatalytic H_2O_2 production efficiencies under different gas bubbling (N_2 , O_2) or scavenger addition (pure water, 10% ethanol, 99.7% ethanol) conditions; (D) cycling runs for the photocatalytic H_2O_2 formation.

higher surface area. The nitrogen adsorption-desorption isotherms of pristine $\text{g-C}_3\text{N}_4$, BCN and CNW-4 are also shown in Fig. S5.† The three samples exhibited type-IV isotherms with a hysteresis loop. Additionally, the pore volumes of pristine $\text{g-C}_3\text{N}_4$, BCN and CNW-4 were obtained to be $0.038733 \text{ cm}^3 \text{ g}^{-1}$, $0.039347 \text{ cm}^3 \text{ g}^{-1}$ and $0.065480 \text{ cm}^3 \text{ g}^{-1}$, respectively. These results indicate that the surface area and porosity have little influence on the enhanced activity of the CNW composites.

The spatial charge separation ability of the CNW-4 composite was also studied by a photoelectrochemical study. Fig. 4(A) presents the photocurrent response of the samples under VL irradiation. It was clear that the CNW-4 sample displays a much higher photocurrent density than pristine $\text{g-C}_3\text{N}_4$ and BCN, suggesting that WSe_2 nanosheets could accelerate the spatial charge separation of $\text{g-C}_3\text{N}_4$. Electrochemical impedance spectroscopy (EIS) was conducted and the results are shown in Fig. 4(B). The Nyquist plots were fitted with a Randles circuit (inset of Fig. 4(B)) which was composed of charge transfer resistance (R_{ct}), electrolyte resistance (R_s), and constant phase elements (CPE). The smaller arc radius of the EIS pattern suggested the more efficient separation of photogenerated e^- - h^+ pairs. It can be observed that the arc radius of CNW-4 is smaller than that of pristine $\text{g-C}_3\text{N}_4$ and BCN, further confirming that the

introduction of WSe_2 nanosheets can increase the interfacial charge-transfer efficiency. In addition, the charge separation efficiency was also examined by the photoluminescence (PL) technique. As presented in Fig. 4(C), for pristine $\text{g-C}_3\text{N}_4$ and BCN, the spectrum shows a strong emission peak at 460 nm, which originates from the band-to-band recombination of electrons and holes. Nevertheless, the intensity of PL was dramatically decreased when loading WSe_2 nanosheets on the surface of $\text{g-C}_3\text{N}_4$, which means that the recombination of electrons and holes was effectively inhibited. To further obtain more information about spatial charge separation and transfer, the time-resolved PL spectra were investigated and the results are shown in Fig. 4(D). It was found that the average PL lifetime was decreased from 5.39 ns to 3.82 ns after incorporating with WSe_2 as the co-catalyst. The decreased lifetime suggested that the radiative recombination of charge pairs was suppressed, and the depopulation of the excited states in the CNW composites occurred more readily through nonradiative pathways, leading to enhanced charge transfer and separation.²¹ Furthermore, the charge transfer efficiency can be calculated from the following equation (eqn (2)):⁵³

$$E = 1 - \frac{\tau_{\text{DA}}}{\tau_{\text{D}}} \quad (2)$$

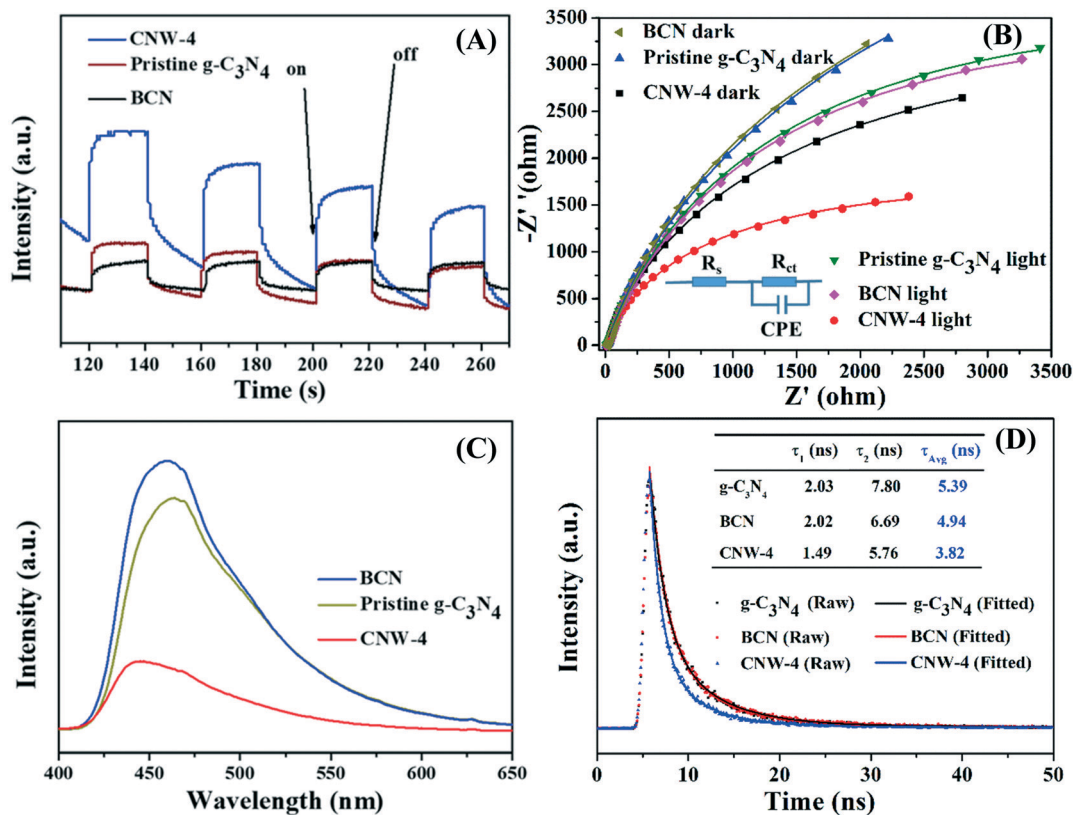


Fig. 4 (A) Transient photocurrent response; (B) electrochemical impedance spectroscopy (EIS) Nyquist plots (inset: fitted with a Randles circuit); (C) photoluminescence (PL) spectra; and (D) time-resolved fluorescence decay spectra of the samples (data were fitted by a double-exponential function).

where τ_{DA} and τ_D are the average PL lifetimes of g-C₃N₄ with and without WSe₂, respectively. The calculated charge transfer efficiency in the CNW composites was obtained to be 29.13%.

To gain insights into the reaction pathway of O₂ reduction, rotating disk electrode (RDE) studies were performed.^{54,55} The linear sweep voltammetry (LSV) measurements indicate that the diffusion-limited current density is increased as the rotation rate changes from 100 to 1800 rpm due to the enhanced diffusion of the electrolyte (Fig. S6(A) and (B)†). The number of electrons involved in the process of O₂ reduction that is calculated from the Koutecky–Levich equation is 2.1–2.54 and 2.35–2.76 for g-C₃N₄ and CNW-4, respectively (Fig. S6(C) and (D)†). This indicates that O₂ reduction over both catalysts is dominated by the 2e pathway. The relatively higher electron-transfer numbers over CNW-4 can be attributed to the enhanced charge transfer at the heterojunction interfaces.⁵⁴

To further reveal the effects of the CNW heterojunctions on the separation of photogenerated e⁻-h⁺ pairs, the band structures of g-C₃N₄ and WSe₂ were studied by analyzing Mott–Schottky plots (Fig. S7(A) and (B)†). As shown, both g-C₃N₄ and WSe₂ present positive slopes of the Mott–Schottky plots, indicating that both samples are typical n-type semiconductors. It shows that the flat-band potential (V_{fb}) of g-C₃N₄ and WSe₂ nanosheets is located at -0.98 V and -1.17 V vs. Ag/AgCl, equivalent to -0.78 V and -0.97 V vs. NHE, respectively. It is generally known that the conduction band (CB) potential is

more negative by approximately -0.1 V than the V_{fb} in n-type semiconductors.⁵⁶ Therefore, the CB of g-C₃N₄ and WSe₂ is located at about -0.88 V and -1.07 V vs. NHE, respectively. Given that the bandgap of g-C₃N₄ and WSe₂ is about 2.70 eV and 1.60 eV,⁵⁷ the valence band (VB) potential of g-C₃N₄ and WSe₂ nanosheets can be calculated to be 1.82 V and 0.53 V vs. NHE, respectively. Obviously, the potential of OH⁻/OH (+1.99 V) is more positive than the VB of g-C₃N₄ and WSe₂ nanosheets. Since the H₂O₂ produced from the VB is believed to be mediated by coupling of [•]OH (eqn (3)),⁵ the lack of [•]OH indicates that the H₂O₂ generation cannot be triggered by photogenerated h⁺ from the VB. However, H₂O₂ is mainly produced *via* the reduction of O₂ by photogenerated e⁻ from the CB (eqn (4)). It should be noted that the CNW composites have a similar CB potential to g-C₃N₄ (Fig. S8†), which suggests that anchoring of WSe₂ nanosheets would not change the band structure of bulk g-C₃N₄.



According to above results, the CB of WSe₂ nanosheets is more negative than that of g-C₃N₄ while the VB of g-C₃N₄ is more positive than that of WSe₂ nanosheets. Therefore, the charge transfer at the CNW interfaces may follow a type II heterojunction mechanism (Fig. S7(C)†) or a Z-scheme

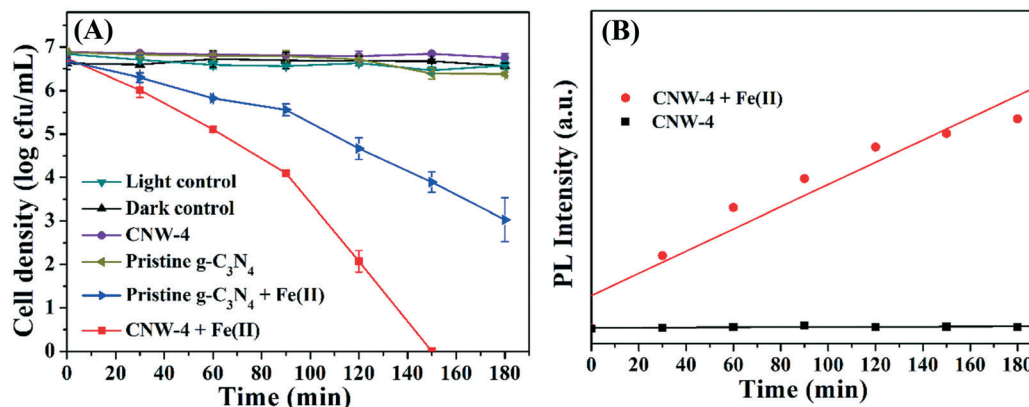


Fig. 5 (A) Photocatalytic bacterial inactivation efficiency with and without Fe(II) (2.7 mM) addition; (B) fluorescence intensity of 7-hydroxycoumarin ([•]OH trapping products) at 460 nm in the CNW-4 and CNW-4/Fe(II) systems.

transfer mode (Fig. S7(D)[†]) under VL illumination. It has been reported that g-C₃N₄ meets the thermodynamic requirements for photocatalytic water oxidation, since its VB potential is located at a value more positive than the H₂O to O₂ oxidation potential (1.23 V vs. NHE).⁵⁸ The photocatalytic water oxidation for O₂ evolution over g-C₃N₄ has also been widely reported in previous studies.^{59–63} In contrast, the VB potential of WSe₂ is insufficient for water oxidation to O₂ evolution. In the present study, the CNW composites can produce O₂ by photocatalytic water oxidation (Fig. S3[†]). Therefore, the photogenerated h⁺ is expected to oxidize water at the VB of g-C₃N₄ rather than WSe₂. In this scenario, the charge transfer should follow the Z-scheme mode rather than the type II transfer mode. In other words, both g-C₃N₄ and WSe₂ nanosheets can be excited with VL irradiation, and then photogenerated e⁻ migrates from the CB of g-C₃N₄ to the VB of WSe₂, forming a Z-scheme type of electron transport. WSe₂ acts as the electron sinker which traps the photogenerated e⁻ from g-C₃N₄. H₂O₂ is then produced at the reduction site of WSe₂, and water oxidation occurs at the oxidation site of g-C₃N₄. The loading of WSe₂ not only facilitates the charge separation, but also promotes the electron energy level at the reduction site, resulting in enhanced photocatalytic H₂O₂ production activity.

3.4 Application in bacterial inactivation

Fig. 5(A) shows *E. coli* inactivation efficiency using the as-prepared samples as photocatalysts under VL irradiation. It was found that both pristine g-C₃N₄ and CNW-4 exhibited very limited activity towards *E. coli* inactivation within 180 min. Surprisingly, the bacterial inactivation efficiency was increased dramatically with the addition of Fe(II). Complete inactivation of 7.0 log cells could be achieved within 150 min in the CNW-4/Fe(II) system, while only 4.0 log-reduction was obtained within 180 min in the g-C₃N₄/Fe(II) system. The inactivation efficiencies coincided with the H₂O₂ production concentrations, suggesting that the generated H₂O₂ was *in situ* activated by added Fe(II) to construct homogeneous Fenton

systems which can be used for bacterial inactivation. To confirm the *in situ* activation of H₂O₂, production of [•]OH was monitored using coumarin as the trapping agent. As shown in Fig. 5(B) and S9[†], the fluorescence intensity of 7-hydroxycoumarin ([•]OH trapping products) increased linearly with reaction time, suggesting that [•]OH was really produced and led to the inactivation of bacterial cells. In contrast, no [•]OH was detected in the CNW-4 sample without Fe(II). This result further confirmed that the produced H₂O₂ could be directly used for bacterial inactivation *via* constructing *in situ* Fenton systems without external addition of H₂O₂.

Based on the above discussion, a possible mechanism for photocatalytic H₂O₂ production for bacterial inactivation over the WSe₂/g-C₃N₄ composite is proposed in Fig. 6. The few layered WSe₂ nanosheets play a critical role in the present photocatalytic H₂O₂ production system, which can efficiently boost the spatial charge separation and suppress the recombination between photogenerated e⁻ and h⁺. The photogenerated e⁻ of g-C₃N₄ transfers to the VB of WSe₂, which improves the enrichment of e⁻ on WSe₂ for H₂O₂

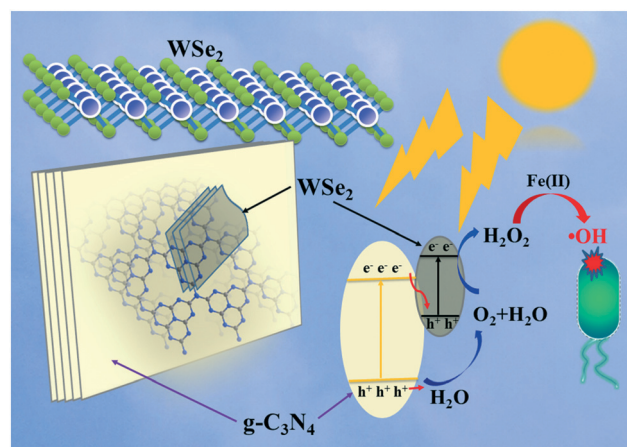


Fig. 6 Schematic illustration of the mechanism for photocatalytic H₂O₂ production for bacterial inactivation in the WSe₂/g-C₃N₄ system under VL irradiation.

production. In addition, the high VL absorption of WSe₂ could facilitate the utilization of photon energy, further improving the H₂O₂ generation efficiency. Moreover, O₂ can be produced by the CNW composite *via* water oxidation, and then can be further used for H₂O₂ production, especially under anaerobic conditions. The produced H₂O₂ can be used for various environmental applications, such as the bacterial inactivation demonstrated in this study, through constructing *in situ* Fenton systems.

4. Conclusions

In summary, few-layered WSe₂ nanosheets were *in situ* anchored onto g-C₃N₄ to construct a binanosheet structure by a solvothermal method. For the first time, the WSe₂/g-C₃N₄ composites were found to be excellent photocatalysts for H₂O₂ production in pure water under VL irradiation. The highest produced H₂O₂ concentration could reach 81.24 μmol L⁻¹ within 2 h in the absence of organic electron donors, which was 11.8 times higher than that of pristine g-C₃N₄. In addition, the generated H₂O₂ could be directly combined with iron catalysts (Fe(II)) to construct *in situ* Fenton systems for bacterial inactivation without addition of external H₂O₂. Complete inactivation of 7.0 log *E. coli* cells could be achieved within 150 min under VL irradiation. These results highlight the potential of using few-layered WSe₂ nanosheets as a general co-catalyst for photocatalytic H₂O₂ production from pure water, thus developing new external oxidant-free Fenton systems for various environmental control applications, for example the degradation of refractory organic pollutants and the inactivation of pathogenic microorganisms, such as bacteria and viruses.

Conflicts of interest

There are no conflicts to declare.

Acknowledgements

This work was supported by the National Natural Science Foundation of China (41425015 and 21607028), the Science and Technology Planning Project of Guangzhou, China (202002030177), the Science and Technology Project of Guangdong Province, China (2017A050506049), the Local Innovative and Research Teams Project of Guangdong Pearl River Talents Program (2017BT01Z032), and the Leading Scientific, Technical and Innovation Talents of Guangdong Special Support Program (2016TX03Z094). The authors are very grateful to Prof. Zhao-Qing Liu (Guangzhou University) for his assistance in conducting the RDE measurements.

References

- 1 S. W. Zhang, H. H. Gao, Y. S. Huang, X. X. Wang, T. Hayat, J. X. Li, X. J. Xu and X. K. Wang, Ultrathin g-C₃N₄ nanosheets coupled with amorphous Cu-doped FeOOH nanoclusters as 2D/0D heterogeneous catalysts for water remediation, *Environ. Sci.: Nano*, 2018, 5, 1179–1190.
- 2 D. H. Kim, A. D. Bokare, M. S. Koo and W. Choi, Heterogeneous catalytic oxidation of As(III) on nonferrous metal oxides in the presence of H₂O₂, *Environ. Sci. Technol.*, 2015, 49, 3506–3513.
- 3 F. Gosselin, L. M. Madeira, T. Juhna and J. C. Block, Drinking water and biofilm disinfection by Fenton-like reaction, *Water Res.*, 2013, 47, 5631–5638.
- 4 J. K. Edwards, B. Solsona, E. N. N. A. F. Carley, A. A. Herzing, C. J. Kiely and G. J. Hutchings, Switching off hydrogen peroxide hydrogenation in the direct synthesis process, *Science*, 2009, 323, 1037–1041.
- 5 Z. Haider, H. I. Cho, G. H. Moon and H. I. Kim, Minireview: Selective production of hydrogen peroxide as a clean oxidant over structurally tailored carbon nitride photocatalysts, *Catal. Today*, 2019, 335, 55–64.
- 6 C. Xia, Y. Xia, P. Zhu, L. Fan and H. Wang, Direct electrosynthesis of pure aqueous H₂O₂ solutions up to 20% by weight using a solid electrolyte, *Science*, 2019, 366, 226–231.
- 7 G. H. Moon, W. Kim, A. D. Bokare, N. E. Sung and W. Choi, Solar production of H₂O₂ on reduced graphene oxide-TiO₂ hybrid photocatalysts consisting of earth-abundant elements only, *Energy Environ. Sci.*, 2014, 7, 4023–4028.
- 8 H. Kim, J. Lim, S. Lee, H. H. Kim, C. Lee, J. Lee and W. Choi, Spontaneous generation of H₂O₂ and hydroxyl radical through O₂ reduction on copper phosphide under ambient aqueous condition, *Environ. Sci. Technol.*, 2019, 53, 2918–2925.
- 9 N. Kaynan, B. A. Berke, O. Hazut and R. Yerushalmi, Sustainable photocatalytic production of hydrogen peroxide from water and molecular oxygen, *J. Mater. Chem. A*, 2014, 2, 13822–13826.
- 10 D. Tsukamoto, A. Shiro, Y. Shiraishi, Y. Sugano, S. Ichikawa, S. Tanaka and T. Hirai, Photocatalytic H₂O₂ production from ethanol/O₂ system using TiO₂ loaded with Au-Ag bimetallic alloy nanoparticles, *ACS Catal.*, 2012, 2, 599–603.
- 11 X. J. Ye, Y. J. Cui, X. Q. Qiu and X. C. Wang, Selective oxidation of benzene to phenol by Fe-CN/TS-1 catalysts under visible light irradiation, *Appl. Catal., B*, 2014, 152, 383–389.
- 12 L. B. Jiang, X. Z. Yuan, G. M. Zeng, J. Liang, Z. B. Wu, H. Wang, J. Zhang, T. Xiong and H. Li, A facile band alignment of polymeric carbon nitride isotype heterojunctions for enhanced photocatalytic tetracycline degradation, *Environ. Sci.: Nano*, 2018, 5, 2604–2617.
- 13 W. Wang, J. C. Yu, D. Xia, P. K. Wong and Y. Li, Graphene and g-C₃N₄ nanosheets cowrapped elemental α-sulfur as a novel metal-free heterojunction photocatalyst for bacterial inactivation under visible-light, *Environ. Sci. Technol.*, 2013, 47, 8724–8732.
- 14 W. Wang, G. Li, T. An, D. K. L. Chan, J. C. Yu and P. K. Wong, Photocatalytic hydrogen evolution and bacterial inactivation utilizing sonochemical-synthesized g-C₃N₄/red phosphorus hybrid nanosheets as a wide-spectral-responsive photocatalyst: The role of type I band alignment, *Appl. Catal., B*, 2018, 238, 126–135.

- 15 W. Wang, T. An, G. Li, D. Xia, H. Zhao, J. C. Yu and P. K. Wong, Earth-abundant Ni₂P/g-C₃N₄ lamellar nanohybrids for enhanced photocatalytic hydrogen evolution and bacterial inactivation under visible light irradiation, *Appl. Catal., B*, 2017, **217**, 570–580.
- 16 J. Li, D. Wu, J. Iocozzia, H. Du, X. Liu, Y. Yuan, W. Zhou, Z. Li, Z. Xue and Z. Lin, Achieving efficient incorporation of pi-electrons into graphitic carbon nitride for markedly improved hydrogen generation, *Angew. Chem., Int. Ed.*, 2019, **58**, 1985–1989.
- 17 M. Liu, S. Wageh, A. A. Al-Ghamdi, P. Xia, B. Cheng, L. Zhang and J. Yu, Quenching induced hierarchical 3D porous g-C₃N₄ with enhanced photocatalytic CO₂ reduction activity, *Chem. Commun.*, 2019, **55**, 14023–14026.
- 18 G. H. Moon, S. Kim, Y. J. Cho, J. Lim, D. H. Kim and W. Choi, Synergistic combination of bandgap-modified carbon nitride and WO₃ for visible light-induced oxidation of arsenite accelerated by in-situ Fenton reaction, *Appl. Catal., B*, 2017, **218**, 819–824.
- 19 S. Zhao and X. Zhao, Insights into the role of singlet oxygen in the photocatalytic hydrogen peroxide production over polyoxometalates-derived metal oxides incorporated into graphitic carbon nitride framework, *Appl. Catal., B*, 2019, **250**, 408–418.
- 20 Y. Shiraiishi, S. Kanazawa, Y. Sugano, D. Tsukamoto, H. Sakamoto, S. Ichikawa and T. Hirai, Highly selective production of hydrogen peroxide on graphitic carbon nitride (g-C₃N₄) photocatalyst activated by visible light, *ACS Catal.*, 2014, **4**, 774–780.
- 21 L. Shi, L. Q. Yang, W. Zhou, Y. Y. Liu, L. S. Yin, X. Hai, H. Song and J. H. Ye, Photoassisted Construction of holey defective g-C₃N₄ photocatalysts for efficient visible-light-driven H₂O₂ production, *Small*, 2018, **14**, 1703142.
- 22 A. Torres-Pinto, M. J. Sampaio, C. G. Silva, J. L. Faria and A. M. T. Silva, Metal-free carbon nitride photocatalysis with in situ hydrogen peroxide generation for the degradation of aromatic compounds, *Appl. Catal., B*, 2019, **252**, 128–137.
- 23 S. N. Li, G. H. Dong, R. Hailili, L. P. Yang, Y. X. Li, F. Wang, Y. B. Zeng and C. Y. Wang, Effective photocatalytic H₂O₂ production under visible light irradiation at g-C₃N₄ modulated by carbon vacancies, *Appl. Catal., B*, 2016, **190**, 26–35.
- 24 R. R. Wang, X. Zhang, F. Li, D. Cao, M. Pu, D. D. Han, J. J. Yang and X. Xiang, Energy-level dependent H₂O₂ production on metal-free, carbon-content tunable carbon nitride photocatalysts, *J. Energy Chem.*, 2018, **27**, 343–350.
- 25 Y. Yang, Z. T. Zeng, G. M. Zeng, D. L. Huang, R. Xiao, C. Zhang, C. Y. Zhou, W. P. Xiong, W. J. Wang, M. Cheng, W. J. Xue, H. Guo, X. Tang and D. H. He, Ti₃C₂ Mxene/porous g-C₃N₄ interfacial Schottky junction for boosting spatial charge separation in photocatalytic H₂O₂ production, *Appl. Catal., B*, 2019, **258**, 117956.
- 26 S. C. Yan, Z. S. Li and Z. G. Zou, Photodegradation of rhodamine B and methyl orange over boron-doped g-C₃N₄ under visible light irradiation, *Langmuir*, 2010, **26**, 3894–3901.
- 27 Y. Shiraiishi, S. Kanazawa, Y. Kofuji, H. Sakamoto, S. Ichikawa, S. Tanaka and T. Hirai, Sunlight-driven hydrogen peroxide production from water and molecular oxygen by metal-free photocatalysts, *Angew. Chem., Int. Ed.*, 2014, **53**, 13454–13459.
- 28 S. Bertolazzi, M. Gobbi, Y. Zhao, C. Backes and P. Samori, Molecular chemistry approaches for tuning the properties of two-dimensional transition metal dichalcogenides, *Chem. Soc. Rev.*, 2018, **47**, 6845–6888.
- 29 A.-J. Cho and J.-Y. Kwon, Hexagonal boron nitride for surface passivation of two-dimensional van der waals heterojunction solar cells, *ACS Appl. Mater. Interfaces*, 2019, **11**, 39765–39771.
- 30 R. S. Guo, Y. T. Han, C. Su, X. W. Chen, M. Zeng, N. T. Hu, Y. J. Su, Z. H. Zhou, H. Wei and Z. Yang, Ultrasensitive room temperature NO₂ sensors based on liquid phase exfoliated WSe₂ nanosheets, *Sens. Actuators, B*, 2019, **300**, 127013.
- 31 L. Zhu, D. C. T. Nguyen, J. H. Woo, Q. F. Zhang, K. Y. Cho and W. C. Oh, An eco-friendly synthesized mesoporous-silica particle combined with WSe₂-graphene-TiO₂ by self-assembled method for photocatalytic dye decomposition and hydrogen production, *Sci. Rep.*, 2018, **8**, 12759.
- 32 M. Biswas, A. Ali, K. Y. Cho and W. C. Oh, Novel synthesis of WSe₂-Graphene-TiO₂ ternary nanocomposite via ultrasonic technics for high photocatalytic reduction of CO₂ into CH₃OH, *Ultrason. Sonochem.*, 2018, **42**, 738–746.
- 33 Z. Y. Lin, J. L. Li, Z. Q. Zheng, L. H. Li, L. L. Yu, C. X. Wang and G. W. Yang, A floating sheet for efficient photocatalytic water splitting, *Adv. Energy Mater.*, 2016, **6**, 1600510.
- 34 X. Duan, C. Wang, A. Pan, R. Yu and X. Duan, Two-dimensional transition metal dichalcogenides as atomically thin semiconductors: opportunities and challenges, *Chem. Soc. Rev.*, 2015, **44**, 8859–8876.
- 35 J. W. Xiao, Y. Zhang, H. J. Chen, N. S. Xu and S. Z. Deng, Enhanced performance of a monolayer MoS₂/WSe₂ heterojunction as a photoelectrochemical cathode, *Nano-Micro Lett.*, 2018, **10**, 60.
- 36 H. Li, Z. J. Peng, J. W. Qian, M. Wang, C. B. Wang and X. L. Fu, C Fibers@WSe₂ nanoplates core-shell composite: Highly efficient solar-driven photocatalyst, *ACS Appl. Mater. Interfaces*, 2017, **9**, 28704–28715.
- 37 W. J. Wang, G. Y. Li, D. H. Xia, T. C. An, H. J. Zhao and P. K. Wong, Photocatalytic nanomaterials for solar-driven bacterial inactivation: recent progress and challenges, *Environ. Sci.: Nano*, 2017, **4**, 782–799.
- 38 X. Wang, J. He, B. Zheng, W. Zhang and Y. Chen, Few-layered WSe₂ in-situ grown on graphene nanosheets as efficient anode for lithium-ion batteries, *Electrochim. Acta*, 2018, **283**, 1660–1667.
- 39 G.-H. Moon, D.-H. Kim, H.-I. Kim, A. D. Bokare and W. Choi, Platinum-like behavior of reduced graphene oxide as a cocatalyst on TiO₂ for the efficient photocatalytic oxidation of arsenite, *Environ. Sci. Technol. Lett.*, 2014, **1**, 185–190.
- 40 W. J. Wang, H. N. Wang, G. Y. Li, T. C. An, H. J. Zhao and P. K. Wong, Catalyst-free activation of persulfate by visible light for water disinfection: Efficiency and mechanisms, *Water Res.*, 2019, **157**, 106–118.

- 41 G. M. Ba, Z. W. Liang, H. P. Li, Q. H. Deng, N. Du and W. G. Hou, Synthesis of hierarchically mesoporous polymeric carbon nitride with mesoporous melamine as a precursor for enhanced photocatalytic performance, *Chem. Eng. J.*, 2020, **380**, 122535.
- 42 T. S. Chen, Q. X. Zhang, X. S. Zheng, Z. J. Xie, Y. Q. Zeng, P. Chen, H. J. Liu, Y. Liu, W. Y. Lv and G. G. Liu, Photocatalyst with a metal-free electron-hole pair double transfer mechanism for pharmaceutical and personal care product degradation, *Environ. Sci.: Nano*, 2019, **6**, 3292–3306.
- 43 M. S. Akple, J. X. Low, S. Wageh, A. A. Al-Ghamdi, J. G. Yu and J. Zhang, Enhanced visible light photocatalytic H₂-production of g-C₃N₄/WS₂ composite heterostructures, *Appl. Surf. Sci.*, 2015, **358**, 196–203.
- 44 J. Xu, G. Dai, B. Chen, D. He, Y. Situ and H. Huang, Construction of Ti³⁺-TiO₂-C₃N₄por compound coupling photocatalysis and Fenton-like process: Self-driven Fenton-like process without extra H₂O₂ addition, *Chemosphere*, 2019, **241**, 125022.
- 45 P. Xia, M. Liu, B. Cheng, J. Yu and L. Zhang, Dopamine modified g-C₃N₄ and its enhanced visible-light photocatalytic H₂-production activity, *ACS Sustainable Chem. Eng.*, 2018, **6**, 8945–8953.
- 46 W. Li, Q. Ma, X. Wang, S.-A. He, M. Li and L. Ren, Hydrogen evolution by catalyzing water splitting on two-dimensional g-C₃N₄-Ag/AgBr heterostructure, *Appl. Surf. Sci.*, 2019, **494**, 275–284.
- 47 B. Yu, B. J. Zheng, X. Q. Wang, F. Qi, J. R. He, W. L. Zhang and Y. F. Chen, Enhanced photocatalytic properties of graphene modified few-layered WSe₂ nanosheets, *Appl. Surf. Sci.*, 2017, **400**, 420–425.
- 48 Z. D. Zhu, H. H. Pan, M. Murugananthan, J. Y. Gong and Y. R. Zhang, Visible light-driven photocatalytically active g-C₃N₄ material for enhanced generation of H₂O₂, *Appl. Catal., B*, 2018, **232**, 19–25.
- 49 S. Zhao, X. Zhao, S. X. Ouyang and Y. F. Zhu, Polyoxometalates covalently combined with graphitic carbon nitride for photocatalytic hydrogen peroxide production, *Catal. Sci. Technol.*, 2018, **8**, 1686–1695.
- 50 L. P. Yang, G. H. Dong, D. L. Jacobs, Y. H. Wang, L. Zang and C. Y. Wang, Two-channel photocatalytic production of H₂O₂ over g-C₃N₄ nanosheets modified with perylene imides, *J. Catal.*, 2017, **352**, 274–281.
- 51 K. Maeda, X. C. Wang, Y. Nishihara, D. L. Lu, M. Antonietti and K. Domen, Photocatalytic activities of graphitic carbon nitride powder for water reduction and oxidation under visible light, *J. Phys. Chem. C*, 2009, **113**, 4940–4947.
- 52 X. F. Yang, L. Tian, X. L. Zhao, H. Tang, Q. Q. Liu and G. S. Li, Interfacial optimization of g-C₃N₄-based Z-scheme heterojunction toward synergistic enhancement of solar-driven photocatalytic oxygen evolution, *Appl. Catal., B*, 2019, **244**, 240–249.
- 53 C. Li, F. Wang, J. Zhu and J. C. Yu, NaYF₄@Yb,Tm/CdS composite as a novel near-infrared-driven photocatalyst, *Appl. Catal., B*, 2010, **100**, 433–439.
- 54 J. Z. Zhang, C. Y. Yu, J. Y. Lang, Y. F. Zhou, B. X. Zhou, Y. H. Hu and M. C. Long, Modulation of Lewis acidic-basic sites for efficient photocatalytic H₂O₂ production over potassium intercalated tri-s-triazine materials, *Appl. Catal., B*, 2020, **277**, 119225.
- 55 S. Zhao, X. Zhao, H. Zhang, J. Li and Y. F. Zhu, Covalent combination of polyoxometalate and graphitic carbon nitride for light-driven hydrogen peroxide production, *Nano Energy*, 2017, **35**, 405–414.
- 56 G. L. Huang, R. Shi and Y. F. Zhu, Photocatalytic activity and photoelectric performance enhancement for ZnWO₄ by fluorine substitution, *J. Mol. Catal. A: Chem.*, 2011, **348**, 100–105.
- 57 C. R. Ryder, J. D. Wood, S. A. Wells and M. C. Hersam, Chemically Tailoring Semiconducting Two-dimensional transition metal dichalcogenides and black phosphorus, *ACS Nano*, 2016, **10**, 3900–3917.
- 58 Z. Wang, C. Li and K. Domen, Recent developments in heterogeneous photocatalysts for solar-driven overall water splitting, *Chem. Soc. Rev.*, 2019, **48**, 2109–2125.
- 59 C. Ye, J. X. Li, Z. J. Li, X. B. Li, X. B. Fan, L. P. Zhang, B. Chen, C. H. Tung and L. Z. Wu, Enhanced driving force and charge separation efficiency of protonated g-C₃N₄ for photocatalytic O₂ evolution, *ACS Catal.*, 2015, **5**, 6973–6979.
- 60 H. Y. Zhang, W. J. Tian, X. C. Guo, L. Zhou, H. Q. Sun, M. O. Tade and S. B. Wang, Flower-like cobalt hydroxide/oxide on graphitic carbon nitride for visible-light-driven water oxidation, *ACS Appl. Mater. Interfaces*, 2016, **8**, 35203–35212.
- 61 G. G. Zhang, S. H. Zang and X. C. Wang, Layered Co(OH)₂ deposited polymeric carbon nitrides for photocatalytic water oxidation, *ACS Catal.*, 2015, **5**, 941–947.
- 62 H. Y. Zhang, W. J. Tian, L. Zhou, H. Q. Sun, M. Tade and S. B. Wang, Monodisperse Co₃O₄ quantum dots on porous carbon nitride nanosheets for enhanced visible-light-driven water oxidation, *Appl. Catal., B*, 2018, **223**, 2–9.
- 63 J. Q. Yan, H. Wu, H. Chen, L. Q. Pang, Y. X. Zhang, R. B. Jiang, L. D. Li and S. Z. Liu, One-pot hydrothermal fabrication of layered β-Ni(OH)₂/g-C₃N₄ nanohybrids for enhanced photocatalytic water splitting, *Appl. Catal., B*, 2016, **194**, 74–83.